Universal relationship between the energy scales of the pseudogap phase, the superconducting state, and the charge-density-wave order in copper oxide superconductors

B. Loret,[1] N. Auvray,[1] G. D. Gu,[2] A. Forget,[3] D. Colson,[3] M. Cazayous,[1] Y. Gallais,[1] I. Paul,[1] M. Civelli,[4] and A. Sacuto[1,*]

[1]*Université de Paris, Laboratoire Matériaux et Phénomènes Quantiques (UMR 7162 CNRS), Bat.Condorcet, 75205 Paris Cedex 13, France*
[2]*Matter Physics and Materials Science, Brookhaven National Laboratory (BNL), Upton, New York 11973, USA*
[3]*Université Paris-Saclay, CEA, CNRS, SPEC, 91191, Gif-sur-Yvette, France*
[4]*Université Paris-Saclay, Laboratoire de Physique des Solides, CNRS, 91405 Orsay Cedex, France*

(Received 18 March 2020; revised manuscript received 2 May 2020; accepted 15 June 2020; published 25 June 2020)

We report the hole doping dependencies of the pseudogap phase energy scale $2\Delta_{PG}$, the antinodal (nodal) superconducting energy scales $2\Delta_{SC}^{AN}$ ($2\Delta_{SC}^{N}$), and the charge-density-wave energy scale $2\Delta_{CDW}$ extracted from the electronic Raman responses of several copper oxide families. We show for all the cuprates studied that the three energy scales $2\Delta_{PG}$, $2\Delta_{SC}^{AN}$, and $2\Delta_{CDW}$ display the same decreasing monotonic behavior with doping. In particular, $2\Delta_{SC}^{AN}$ and $2\Delta_{CDW}$ have nearly equal values. This suggests a universal scenario in which $2\Delta_{PG}$, $2\Delta_{SC}^{AN}$, and $2\Delta_{CDW}$ are governed by common microscopic interactions that become relevant well above the superconducting transition at T_c. This is to be contrasted with the behavior of the nodal superconducting energy scale $2\Delta_{SC}^{N}$, which tracks the doping dependence of T_c and, hence, seems to be controlled by different interactions.

DOI: 10.1103/PhysRevB.101.214520

I. INTRODUCTION

The copper oxide (cuprate) superconductors are materials with an extremely rich temperature-doping (T-p) phase diagram. By decreasing T, a mysterious phase is established, the pseudogap (PG) which manifests itself by the suppression of low energy electronic states. By further reducing temperature, a charge-density-wave (CDW) order settles down. Finally, at lower T superconductivity (SC) arises [1]. The overriding question that remains unanswered since the discovery of superconductivity in cuprates by Bednorz and Muller in 1986 [2] is what are the underlying quantum electronic orders that control the (T-p) cuprate phase diagram? This question leads to other recurring questions such as the following. Why is the doping dependencies of the superconducting transition temperature $T_c(p)$ and the charge-density-wave transition temperature $T_{CDW}(p)$ domelike? Why instead does the pseudogap temperature $T^*(p)$ decreases linearly as p increases? In order to address these key questions it is essential to identify the relation between the transition temperatures $T_c(p)$, $T_{CDW}(p)$, and $T^*(p)$ and the corresponding energy scales, $2\Delta_{SC}^{AN}$ ($2\Delta_{SC}^{N}$), $2\Delta_{CDW}$, and $2\Delta_{PG}$. Here AN and N refer to antinodal and nodal regions corresponding to the principal axes and the diagonal of the first Brillouin zone (BZ), respectively. For mean field type second order phase transitions, such as superconducting transitions in conventional systems [3], the transition temperature is proportional to the associated energy scale of the order parameter, such as the gap value. As we discuss in detail below, this is not the case either for the superconducting or the charge-density-wave transitions of the cuprates, which emphasizes their unconventional nature.

The scope of this article is to determine the above mentioned energy scales of various cuprate families, extending our previous work on trilayered $HgBa_2Ca_2Cu_3O_{8+\delta}$ [4]. The goal here is to show that their relation with the transition temperatures and their behavior as a function of doping are universal features of the cuprate phase diagram. Our findings also provide important clues on the relationship between the different quantum electronic orders.

Our study is based on the electronic Raman spectroscopy (ERS), which is a very effective probe to track the energy scales of the superconducting gap, the pseudogap [5–12], or more recently the charge-density-wave gap [4]. Since ERS is a two photon scattering process, by controlling the incoming and outgoing photon polarizations, one can selectively probe different regions of the BZ. Thus, in the B_{1g} geometry the Raman form factor is $(\cos k_x - \cos k_y)^2$ and it predominantly probes the antinodal region. Here $\mathbf{k}$ is the wave vector of the excited electron. Likewise, in the B_{2g} geometry the Raman form factor is $\sin^2 k_x \sin^2 k_y$ and it probes mostly the nodal region. This form factor induced momentum space selectivity is particularly useful for studying the cuprates, since it is well known that the electronic properties in the antinodal and nodal regions are quite different [13]. Thus, both the superconducting gap and the pseudogap energy scale are maximal around the antinode, and minimal around the nodal region. Furthermore, since the energy gaps from pseudogap is minimal in the nodal region, we find that any additional loss of low-energy spectral weight due to the formation of the charge-density wave is readily detected in the B_{2g} geometry, and not in the B_{1g} geometry where the signal of the

*Corresponding author: alain.sacuto@univ-paris-diderot.fr

charge-density wave is masked by the pseudogap. Yet another useful aspect of ERS is that it is a frequency resolved, but (form factor weighted) momentum averaged probe. Therefore it is quite sensitive to gap opening due to a short range order, as is the case of the charge-density wave in the cuprates in the absence of magnetic field. This is because any spatial variation of the ordering wave vector in a short range order does not blur the energy gap feature in frequency space if the probe is frequency resolved [14]. The ERS measurements were performed on four distinct cuprates: $HgBa_2CuO_{4+\delta}$ (Hg-1201), $YBa_2Cu_3O_{6+\delta}$ (Y-123), $Bi_2Sr_2CaCu_2O_{8+\delta}$ (Bi-2212), and $HgBa_2Ca_2Cu_3O_{8+\delta}$ (Hg-1223). In our previous study [4] we determined the doping dependence of the energy scales of the Hg-1223 compound and the doping trend of the CDW energy scale of Y-123 compounds. Here, among the new results, we were able to identify the CDW energy scale and the doping dependence of the PG energy scale in Bi-2212 compound. We also succeeded in following the doping dependence of the CDW energy scale in Hg-1201 compound by reinterpreting the Raman data obtained from another group [15]. This allows us to obtain a universal picture of the doping evolution of the energy scales over several cuprates. We find that $2\Delta_{PG}$, $2\Delta_{SC}^{AN}$, and $2\Delta_{CDW}$ have the same doping dependency as $T^*(p)$, they decrease linearly with doping. This suggests that they are all driven by the same microscopic mechanism. We also find that the $2\Delta_{PG}$ is approximately twice larger than $2\Delta_{SC}^{AN}$ and $2\Delta_{CDW}$ which are instead very close to each other. This suggests first that $2\Delta_{PG}$ scale (detected here) cannot be ascribed to SC fluctuations [16] (since it is too far from the SC gap scale $2\Delta_{SC}^{AN}$). Second and most importantly, this indicates that the SC and CDW orders are intimately connected (since $2\Delta_{SC}^{AN} \approx 2\Delta_{CDW}$) and deserve to be investigated in the light of recent theoretical models such as composite or intertwined orders [17–22].

II. ANTINODAL SUPERCONDUCTING AND PSEUDOGAP ENERGY SCALES

Our first goal is to show how we can detect and define the energy scales of the antinodal part of the SC gap and the PG phase in cuprates. As an illustration, we present the B_{1g} Raman responses of the underdoped Hg-1223 (UD 117) and Bi-2212 (UD 122 75) compounds. The number in parentheses corresponds to the T_c value. As mentioned above, the B_{1g} geometry in Raman spectroscopy gives us access to the antinodal part of the BZ. The details of the ERS experimental procedure is given in Appendix A. Details on the crystals growth, the $T_c$values, and doping are given in Appendix B.

In Figs. 1(a) and 1(b) the SC Raman responses of Hg-1223 (UD 117) and Bi-2212 (UD 75) at 12 K exhibit a well defined pair breaking peak $2\Delta_{SC}^{AN}$ at approximately two times the energy of the SC gap measured by tunneling and angular resolved photoemission spectroscopy (ARPES). It corresponds to the maximum amplitude of the d-wave SC gap probed at the antinodes. It is located around 1500 and 570 cm^{-1} for Hg-1223 (UD 117) and Bi-2212 (UD 75), respectively, and marked by a red arrow. The $2\Delta_{SC}^{AN}$ peak is associated on its high energy side with a dip in the electronic continuum. The dip is revealed by comparing the SC (at 12 K) and the

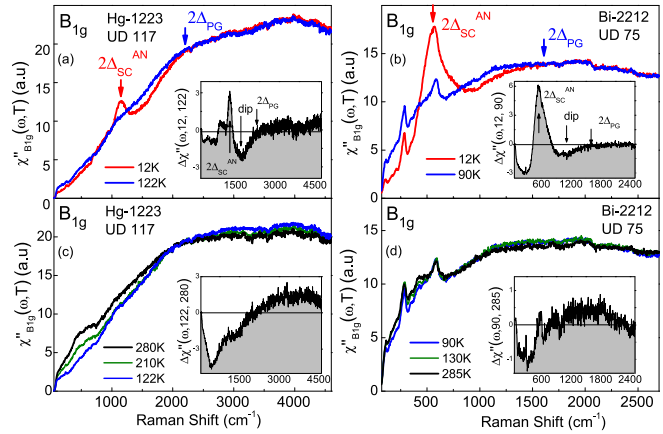

FIG. 1. For $T \leqslant T_c$, B_{1g} (antinodal) Raman response functions of (a) an underdoped Hg-1223 (UD 117, $p \approx 0.12$) and (b) Bi-2212 (UD 75, $p \approx 0.11$) single crystal. (c) and (d) For $T \geqslant T_c$. The SC energy scale $2\Delta_{SC}$ and the PG energy scale $2\Delta_{PG}$ are indicated by a red and blue arrow, respectively. In the insets of (a) and (b), the subtracted Raman response (defined in the text) underlines the peak-dip structure. In the insets of (c) and (d), the subtracted Raman response (defined in the text), points out the spectral weight transfer induced by the pseudogap phase in the normal state. The shaded area allows by contrast a better visualization of the peak-dip structure in the SC state and the spectral weight transfer in the normal state.

normal Raman responses just above T_c [122 K for Hg-1223 (UD 117) and 90 K for Bi-2212 (UD 75)]. In previous works we showed that this peak-dip structure detected in the superconducting B_{1g} Raman response results from the interplay between the PG and the SC gap [11,12,23]. The peak-dip structure is emphasized by the subtracted Raman responses $\Delta\chi''_{B_{1g}}(\omega, 12\ \text{K}, 122\ \text{K}) = \chi''_{B_{1g}}(\omega, 12\ \text{K}) - \chi''_{B_{1g}}(\omega, 122\ \text{K})$ and $\Delta\chi''_{B_{1g}}(\omega, 12\ \text{K}, 90\ \text{K})$ for Hg-1223 (UD 117) and Bi-2212 (UD 75), respectively [see insets of Figs. 1(a) and 1(b)]. We established (i) that the peak-dip structure is only detected when the pseudogap exists [11,12,23] and (ii) it can be smoothly connected to the loss of spectral weight related to the PG above T_c (see Appendix C). Above T_c, as the temperature is lowered, see Figs. 1(c) and 1(d), we observe simultaneously a loss and a slightly increase of spectral weight of the electronic background below and above 2000 and 1000 cm^{-1} for, respectively, Hg-1223 (UD 117) and Bi-2212 (UD 75). This is due to a quasiparticles spectral weight transfer from low to high frequency which characterizes the pseudogap phase. This is underlined by the subtracted Raman responses $\Delta\chi''_{B_{1g}}(\omega, 122\ \text{K}, 280\ \text{K})$ [for Hg-1223 (UD 117)] and $\Delta\chi''_{B_{1g}}(\omega, 90\ \text{K}, 285\ \text{K})$ [for Bi-2212 (UD 75)] which signal the loss and the increase of the spectral weight in the negative and positive part of the spectra, respectively, as shown in the insets of Figs. 1(c) and 1(d). In the positive part of the spectra, it is hard to accurately define an energy scale for the PG in the normal state, because the hump is almost flat on a large frequency range (2500–4500 cm^{-1}) and (800–2000 cm^{-1}) for Hg-1223 (UD 117) and Bi-2212 (UD 75), respectively. On the other hand, the energy of the dip end of the SC B_{1g} response is more easily detectable and since it corresponds to the Raman signature of the PG in the SC

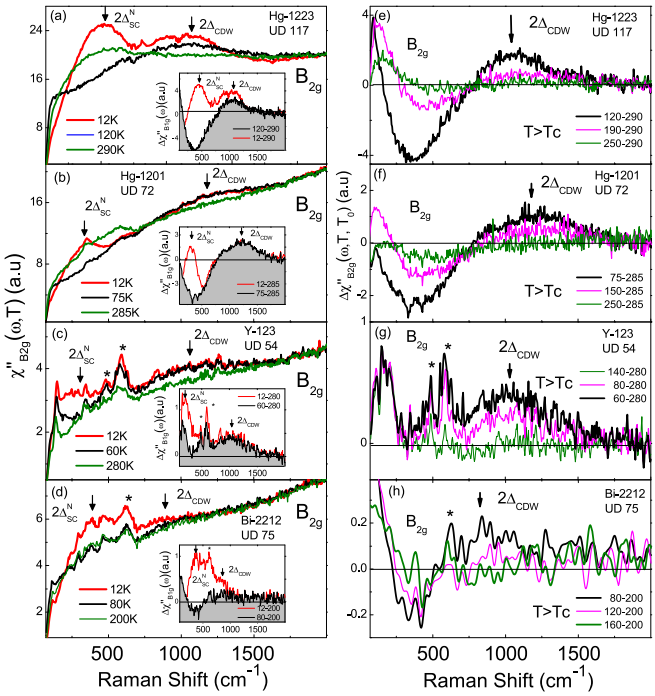

FIG. 2. B_{2g} (nodal) Raman response functions of Hg-1223 (UD 117, $p \approx 0.12$), Hg-1201 (UD 72, $p \approx 0.11$), Y-123 (UD 54, $p \approx 0.08$), and Bi-2212 (UD 75, $p \approx 0.11$) compounds. (a)–(d) Selected temperatures above and below T_c. In the insets we plot the subtractions between the Raman responses measured below (red curve) and just above (black curve) T_c and the ones measured at T_0. $T_0 = 290$, 285, 280, and 200 K for Hg-1223, Hg-1201, Y-123, and Bi-2212, respectively. The shaded area allows a better visualization of the CDW signal. (e)–(h) Subtracted Raman responses between selected temperatures above T_c and T_0. The peaks labeled by a star in the Y-123 and Bi-2212 are phonon modes induced by oxygen disorder [31,32]. Note that since the CDW signal is intrinsically weak in the Bi-2212 compound, we applied a slight filtering by using Fourier transform to improve the signal noise ratio of the Raman response in (h).

state [4,11,12,23], we defined it as the PG energy scale $2\Delta_{PG}$ marked by a blue arrow in Fig. 1. $2\Delta_{PG}$ corresponds to the high energy pseudogap detected in the tunneling and ARPES measurements [24–26] and discussed in Ref. [27]. The $2\Delta_{SC}^{AN}$ and $2\Delta_{PG}$ scales for the Y-123 and Hg-1201 compounds were obtained using the same method (analyzing the peak-dip structure in the SC Raman response [11]). All the energy scales that we have measured by ERS for the various cuprates are shown in Fig. 3. We have also defined the pseudogap temperature T^* by the temperature at which the transfer of spectral weight from low to high energies detected in the B_{1g} Raman response ceases. The T^* values that we obtained are in agreement with those obtained from other techniques, and are reported in Fig. 3.

III. NODAL SUPERCONDUCTING AND CHARGE-DENSITY-WAVE ENERGY SCALES

We investigate now the energy scales of the nodal SC gap and the CDW order. The B_{2g} geometry in Raman spectroscopy allows us to capture the electronic states located in the nodal region of the first BZ, it is therefore well adapted to study the nodal component of the superconducting gap. On the other hand, the parts of the Fermi surface which are expected to be the most affected by the CDW order are located in between the nodal and the antinodal regions [28], meaning that they are potentially accessible by both the B_{1g} or B_{2g} geometry. However, since T_{CDW} is below T^*, the CDW signal close to the antinodes may be affected or masked by the pseudogap spectral weight loss. It is therefore more adapted to look for the CDW signal close to the nodes, where the pseudogap effect is known to be minimal. In our previous investigations we have mostly investigated the CDW signal in Hg-based compounds [4]. Here we show that we are also able to detect the CDW signal also in Y-123 and Bi-2212 compounds, despite the presence of few phonon modes which are not detected in Hg-based compounds. So we have studied the B_{2g} Raman response of the four following cuprates: Hg-1223 (UD 117), Hg-1201 (UD 72), Y-123 (UD 54), and Bi-2212 (UD 75). The details of the crystal growths and characterizations of Hg-1201 and Y-123 can be found in Refs. [29,30].

Below T_c [red curves in Figs. 2(a) to 2(d)], we detect two distinct features arrowed $2\Delta_{SC}^{N}$ and $2\Delta_{CDW}$ in the Raman spectra of Hg-1223, Hg-1201, Y-123, and Bi-2212. These features are highlighted by the subtracted Raman responses $\Delta\chi''_{B_{2g}}(\omega, T = 12\ \text{K}, T_0)$ obtained from the difference between the Raman responses taken at $T = 12$ K and the ones measured at $T_0 > T_c$ [see red curves in the insets of Figs. 2(a) to 2(d)]. T_0 is defined in the caption of Fig. 2. The extra narrow features labeled by a star in Fig. 2 correspond to phonon lines (see caption of Fig. 2). The $2\Delta_{SC}^{N}$ peak located at 470 cm^{-1} for Hg-1223, 300 cm^{-1} for Hg-1201, 250 cm^{-1} for Y-123, and 372 cm^{-1} for Bi-2212, disappears above T_c. This feature is assigned to the well known nodal component of the d-wave SC gap and already extensively studied in Y-123, Bi-2212, and Hg-1201 [6,7,33,34]. On the contrary, $2\Delta_{CDW}$, located at a higher frequency than $2\Delta_{SC}^{N}$, persists above T_c [see black curves in the insets of Figs. 2(a) to 2(d)] and exhibits a maximum around 1000 cm^{-1} for Hg-1223 (UD 117), 1150 cm^{-1} for Hg-1201 (UD 72), 1000 cm^{-1} for Y-123 (UD 54), and 850 cm^{-1} for Bi-2212 (UD 75). We define the position of the maximum of the hump as the CDW energy scale $2\Delta_{CDW}$ which has been first identified in Ref. [4] for Hg-1223. All these energy scales are reported in Fig. 3. By raising the temperature above T_c, the CDW hump progressively decreases in intensity. This is pointed out by looking at the subtracted Raman responses $\Delta\chi''_{B_{2g}}(\omega, T > T_c, T_0)$ of Hg-1223, Hg-1201, Y-123, and Bi-2212 [Figs. 3(e)–3(h)]. They exhibit a dip-hump structure characteristic of the CDW spectral weight transfer that disappears with increasing T. We have defined T_{CDW} as the temperature at which the integrated Raman intensity of the CDW hump vanishes. The T_{CDW} values of Hg-1223, Hg-1201, Y-123, and Bi-2212 (UD 75) are reported in Fig. 3 and are in agreement with those obtained from other techniques, see Fig. 3. At this stage it is important to notice that although T_{CDW} has been extensively mapped out in several cuprates, only very few data have been reported on the $2\Delta_{CDW}$ energy scale. One can then legitimately wonder whether the CDW signal we observed in B_{2g} geometry is

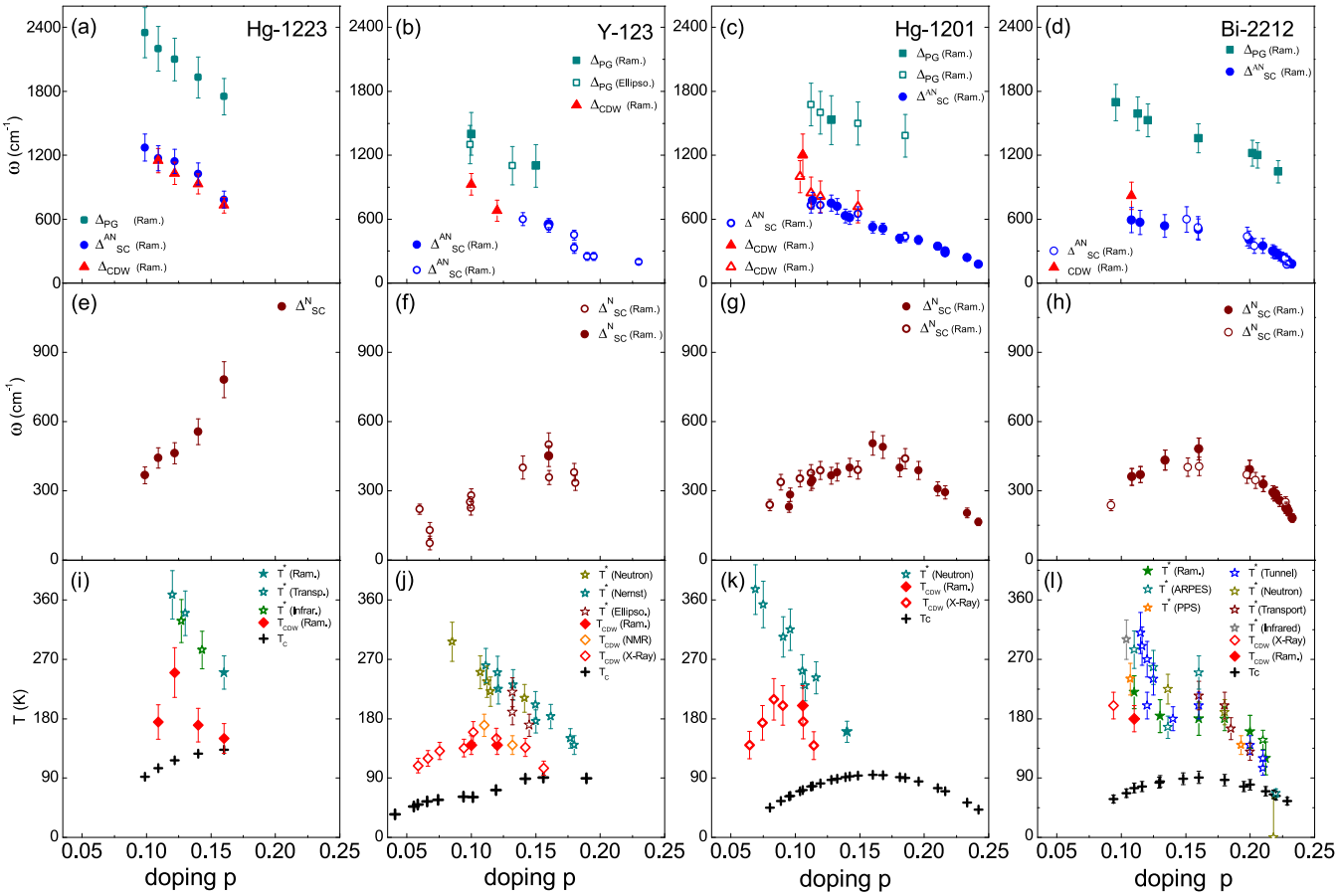

FIG. 3. Universal doping dependencies of the pseudogap, the antinodal superconducting, and the charge-density-wave energy scales [respectively $2\Delta_{\mathrm{PG}}(p)$, $2\Delta_{\mathrm{SC}}^{\mathrm{AN}}(p)$, and $2\Delta_{\mathrm{CDW}}(p)$] over four cuprates systems: (a) Hg-1223, (b) Y-123, (c) Hg-1201, and (d) Bi-2212 cuprates. (e)–(h) The doping dependence of the nodal superconducting energy scale $2\Delta_{\mathrm{SC}}^{\mathrm{N}}(p)$ for Hg-1223, Y-123, Hg-1201, and Bi-2212, respectively. (i)–(l) The doping dependence of the relevant transition temperatures: the pseudogap T^*, the superconducting T_c, and the charge-density-wave T_{CDW} for Hg-1223, Y-123, Hg-1201, and Bi-2212, respectively. The filled symbols correspond to our Raman data. Our data on Y-123, Hg-1201, and Bi-2212 are supplemented by Raman measurements from other groups (designated by empty symbols), see Ref. [37].

also detected by other spectroscopic techniques in the Bi-2212 compound. We can effectively find that polarized pump probe measurements have reported such signals at nearly the same energy [35]. Additionally, ARPES measurements report a gap opening in the nodal region (B_{2g} geometry) below T^* which could be related to a CDW order [36].

IV. UNIVERSAL DOPING DEPENDENCE OF THE ENERGY SCALES IN SEVERAL CUPRATES AND ITS RELATIONSHIP ON THE CUPRATES PHASE DIAGRAM

Having showed how to extract and identify the energy scales of the SC state, the PG phase, and the CDW order from the electronic Raman response, our objective is to track their doping dependencies for various families of cuprates that we studied, and see if there exists some common trends and how they can eventually be connected on the cuprate phase diagram. By way of illustration we have reported in Appendix D the Raman responses of the Hg-1223 compound for several doping levels from which we extracted the energy scales: $2\Delta_{\mathrm{SC}}^{\mathrm{AN}}$, $2\Delta_{\mathrm{PG}}$, $2\Delta_{\mathrm{SC}}^{\mathrm{N}}$, and $2\Delta_{\mathrm{CDW}}$. The doping dependence of these four energy scales are shown in Figs. 3(a) and 3(e) for Hg-1223, Figs. 3(b) and 3(f) for Y-123, Figs. 3(c) and 3(g) for Hg-1201, and Figs. 3(d) and 3(h) for Bi-2212 [37]. Remarkably we find universal trends in the doping dependencies of the above energy scales. The PG, AN-SC, and CDW energy scales decrease linearly as p increases on a substantial doping range [Figs. 3(a)–3(d)] in all these cuprate families. The $2\Delta_{\mathrm{PG}}$ scale is about twice as large as that of the $2\Delta_{\mathrm{SC}}^{\mathrm{AN}}$ and $2\Delta_{\mathrm{CDW}}$ scales which are found to be very close to each other. On the contrary, the $2\Delta_{\mathrm{SC}}^{\mathrm{N}}$ scale is nonmonotonic, it increases with doping up to the optimal doping level ($p = 0.16$) [see Figs. 3(e)–3(h)] and then it decreases in the overdoped regime ($p \geqslant 0.16$). As a result, the $2\Delta_{\mathrm{SC}}^{\mathrm{N}}(p)$ has a domelike shape fully observed in Figs. 3(g) and 3(h) for Hg-1201 and Bi-2212. If we now venture into a comparison between the doping dependence of these energy scales and the T-p cuprate phase diagram [see Figs. 3(i)–3(l)], the salient experimental facts are that $2\Delta_{\mathrm{PG}}(p)$ and the $2\Delta_{\mathrm{SC}}^{\mathrm{N}}(p)$ follow the same behavior as $T^*(p)$ and $T_c(p)$, respectively, while $2\Delta_{\mathrm{CDW}}(p)$ and $2\Delta_{\mathrm{SC}}^{\mathrm{AN}}(p)$ do not follow $T_{\mathrm{CDW}}(p)$ and $T_c(p)$, respectively. At this stage we are not in a position to propose a theory that would allow us to fully understand the doping dependencies of the energy scales and their correspondences with the characteristic temperatures of the cuprate phase diagram. However, if we focus on the

doping dependency of the energy scales, we can draw some key observations from it. We can first hypothesize that the three energy scales (PG, AN-SC, and CDW) have probably a common microscopic origin since they have the same doping dependence. They decrease monotonically with doping as expected, e.g., for the singlet formation energy in the resonant valence bound (RVB) model [38]. Their microscopic origin could be, e.g., short range antiferromagnetic fluctuations [39] which decrease as one moves away by doping from Mott insulating antiferromagnetic phase [40–48]. We can also reasonably say that since $2\Delta_{PG}(p)$ is at least twice as large as $2\Delta_{SC}^{AN}(p)$, it cannot be assigned to superconducting fluctuations as proposed by a preformed pair scenario [16]. Another point worth mentioning is the same doping dependence of the N-SC and T_c as opposed to the AN-SC gap that does not follow T_c. This suggests that nodal quasiparticles are likely not subject to the same electronic interactions governing quasiparticles at the antinodes. On the other hand, the close values of the AN-SC and CDW energy scales, which we report here in several cuprates [Figs. 3(a)–3(d)], is a surprising fact that deserves to be explored in the light of recent theoretical models of intertwined or composite orders [17–22].

V. CONCLUSION

In conclusion, we have determined the universal energy scales behavior associated with the the T-P cuprate phase diagram by extracting from electronic Raman scattering measurements the energy scales of the PG phase, of the antinodal and nodal superconducting state, and of the charge-density-wave order for several cuprates families (Hg-1223, Hg-1201, Y-123, and Bi-2212). In all these cuprates we find that $\Delta_{PG}(p)$, $2\Delta_{SC}^{AN}(p)$, and $2\Delta_{CDW}(p)$ have the same doping dependence as $T^*(p)$: they decrease monotonically with doping. This suggests that they are all driven by the same microscopic interactions which could come for instance, from short range antiferromagnetic fluctuations. The closeness of the AN-SC and CDW energy scales suggests that these orders are intimately connected and that the pseudogap phase could be considered as intertwined or composite order of particle-particle and particle-hole pairs [17–22]. On the contrary, the nodal component of the SC gap $2\Delta_{SC}^{N}(p)$, which follows the same doping dependence as $T_c(p)$, does not appear to be affected by any of the above interactions. Our experimental results will motivate future theoretical advancements that could account for these universal energy scales of the cuprate phase diagram.

ACKNOWLEDGMENTS

We are grateful to V. Brouet, A. Carrington, A. Chubukov, R. M. Fernandes, E. Fradkin, A. Georges, G. Ghiringhelli, M. Greven, M. Grilli, M.-H. Julien, M. Le Tacon, A. Mesaros, C. Pépin, C. Proust, Y. Sidis, L. Taillefer, A. M. Tremblay, and P. Volkov for useful discussions. We thank the University of Paris, the Collège de France, and the Canadian Institute for Advanced Research (CIFAR) for their support. B.L. was supported by the DIM OxyMORE, Ile de France. The work at Brookhaven National Laboratory was supported by the Office of Science, U.S. Department of Energy under Contract No. DESC0012704.

APPENDIX A: DETAILS OF THE ELECTRONIC RAMAN EXPERIMENTS

Raman experiments have been carried out using a JY-T64000 spectrometer in single grating configuration using a 600 grooves/mm grating and a Thorlabs NF533-17 notch filter to block the stray light. The spectrometer is equipped with a nitrogen cooled back illuminated 2048×512 CCD detector. We use the 532 nm excitation line from a diode pump solid state with laser power maintained at 4 mW. Measurements between 10 and 290 K have been performed using an ARS closed-cycle He cryostat. This configuration allows us to cover a wide spectral range (90 to 2500 cm^{-1}) with a resolution sets at 5 cm^{-1}. Spectra have been obtained from a single frame. Each frame is repeated twice to eliminate cosmic spikes and acquisition time is about 20 min. All the spectra have been corrected for the Bose factor and the instrumental spectral response. They are thus proportional to the imaginary part of the Raman response function $\chi''(\omega, T)$. The B_{1g} symmetry is obtained from crossed polarizations along the Cu-O bond directions. Then the crystal is rotated by 45° using a Attocube piezorotator ANR 101 to obtain the B_{2g} symmetry always using crossed polarizations. The B_{1g} symmetry probes mostly the principal axes of the BZ (antinodal region), and it corresponds to the maximum amplitude of the SC gap, while the B_{2g} symmetry probes mainly the diagonal of the BZ (nodal region), and it corresponds to the region where the amplitude of the d-wave SC gap vanishes.

APPENDIX B: DETAILS ON THE CRYSTAL GROWTH, DOPING, AND CRITICAL TEMPERATURE OF HG-1223 AND BI-2212 SINGLE CRYSTALS

1. Hg-1223

The Hg-1223 single crystals were grown by a single step synthesis [49]. The as-grown single crystal has a critical temperature $T_c \approx 110$ K. T_c has been changed by annealing the single crystal under vacuum or oxygen. A thorough x-ray diffraction analysis reveals that oxygen atoms are removed (for underdoping) or added (for overdoping) inside the Hg layer [50]. The doping levels were estimated from the empirical Presland-Tallon's law [51]. The single crystals are parallelepiped with a typical cross section of 0.7×0.7 mm^2 and a thickness of 0.2 mm. The c axis is normal to the surface with the a-b plane directions 45° from the edges. In order to have high optical quality surface, the crystals have been polished using diamond paste at 1/10 μm. DC magnetization measurements under zero field cooling (ZFC) have been performed after polishing and displayed in Fig. 4(a). The transition temperature T_c and its width ΔT_c was estimated by taking the maximum and the full width at half maximum of the peak of the first derivative of each DC magnetization curve shown in Fig. 4(b). The T_c and ΔT_c values for each doping are the following: $p = 0.16$ ($T_c = 133$ K, $\Delta T_c = 1$ K), $p = 0.14$ ($T_c = 127$ K, $\Delta T_c = 1.5$ K), $p = 0.12$ ($T_c = 117$ K, $\Delta T_c = 5$ K), $p = 0.11$ ($T_c = 105$ K, $\Delta T_c = 4$ K), $p = 0.94$ ($T_c = 92$ K, $\Delta T_c = 7$ K). ΔT_c broadens when we move away from the optimal doping level. This reflects slightly doping inhomogeneity in the single crystal with underdoping.

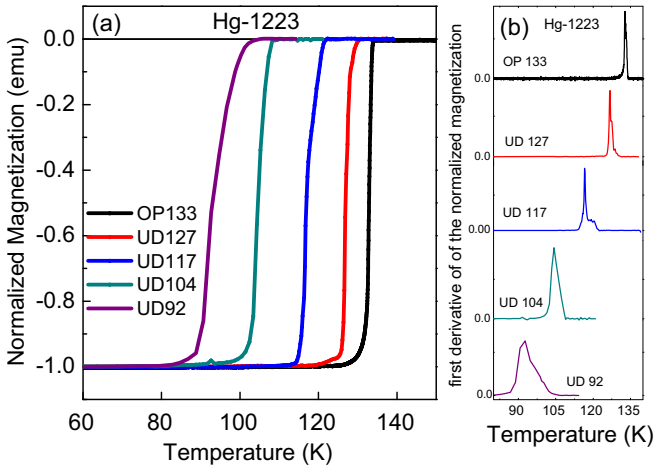

FIG. 4. (a) Zero field cooling magnetization curves of Hg-1223 single crystals for several doping levels. The applied magnetic field is perpendicular to the *ab* plane and its magnitude is of ≈ 10 Oe. (b) First derivative of the magnetization curves displayed in (a). The location of the peak maximum indicates the value of T_c and its full width at half maximum the transition width.

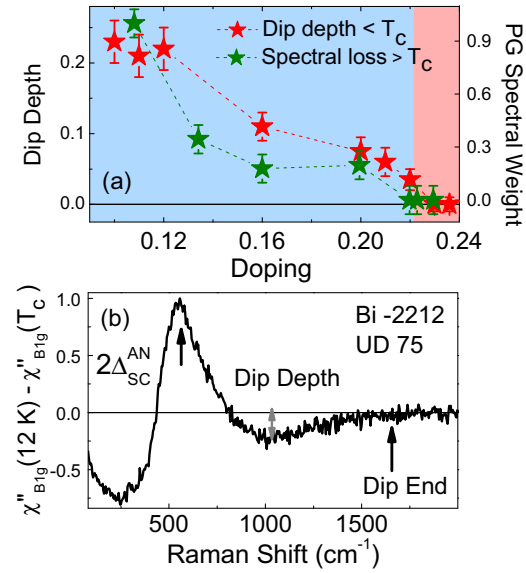

FIG. 5. (a) Doping evolution of the dip depth and the loss of spectral weight generated by the pseudogap phase. (b) Characteristic peak-dip structure extracted from the subtracted Raman response of Bi-2212 (UD 75) single crystal between the SC and the normal state just above T_c.

2. Bi-2212

The Bi-2212 single crystals were grown by using a floating zone method. The optimal doped sample with $T_c = 90$ K was grown at a velocity of 0.2 mm/h in air [52]. In order to get overdoped samples down to $T_c = 65$ K, the as-grown single crystal was put into a high oxygen pressured cell between 1000 and 2000 bars and then was annealed from 350 to 500 °C during 3 days [53]. The overdoped samples below $T_c = 60$ K were obtained from as-grown Bi-2212 single crystals put into a pressure cell (Autoclave France) with 100 bars oxygen pressure and annealed from 9 to 12 days at 350 °C. Then the samples were rapidly cooled down to room temperature by maintaining a pressure of 100 bars. The critical temperature T_c for each crystal has been determined from magnetization susceptibility measurements at a 10 G field parallel to the c axis of the crystal. In the overdoped regime, T_c increases linearly with $2\Delta_{SC}^{AN}$. From a linear fit of the T_c values between $T_c = 50$ K and $T_c = 90$ K, we find the reliable relationship: $T_c = (2\Delta_{SC}^{AN})/8.2 + 28.6$ [10]. In the underdoped regime T_c falls down abruptly as a function of $2\Delta_{SC}^{AN}$ (see Fig. 5). The level of doping p was defined from T_c using Presland and Tallon's equation [51]: $1 - T_c/T_c^{max} = 82.6(p - 0.16)^2$. In the overdoped regime, estimate of p can be determined from $2\Delta_{SC}^{AN}$ using the above two equations.

APPENDIX C: CONNECTION BETWEEN THE DIP STRUCTURE IN THE SUPERCONDUCTING STATE AND THE NORMAL STATE PSEUDOGAP

In order to show that there is a direct link between the dip structure detected in the SC state Raman response and the spectral weight loss detected in the normal state Raman response when the pseudogap phase settles down, we have simultaneously plotted [see Fig. 5(a)] the doping evolution of the dip and the loss of spectral weight in the Raman spectra of Bi-2212. The characteristic elements of the peak-dip structure measured on Bi-2212 (UD 75) are defined in Fig. 5(b). We quantified the dip depth from the subtracted Raman response measured at low temperature (≈ 12 K) in the SC state and just above T_c. The loss of spectral weight is defined in Ref. [10]. From Fig. 5(a) it clearly appears that the dip depth and the loss of spectral weight are associated with the pseudogap phase. These results are supported by cellular dynamical mean field theory calculations (see the Appendix in Ref. [11]).

APPENDIX D: EXTRACTION OF THE ENERGY SCALES FROM THE RAMAN RESPONSE OF HG-1223 SYSTEMS

1. Superconducting antinodal and pseudogap energy scales versus doping

The Δ_{SC}^{AN} scale is the maximum energy of the d wave SC gap which takes place in the antinodal region of the BZ. It is therefore experimentally observed in the B_{1g} Raman response. In fact, we are detecting twice the superconducting gap energy $2\Delta_{SC}^{AN}$ which corresponds to the frequency of the pair breaking peak indicated by a red arrow in the top panels of Figs. 6(a) and 6(c) and Figs. 6(e) and 6(g). We see that $2\Delta_{SC}^{AN}$ decreases in intensity and increases in frequency as p is lowering from 0.16 to 0.10. This doping dependence is a common feature to all the cuprates studied (cf. Fig. 3). Its rapid intensity decrease is likely due the loss of the spectral weight in the antinodal region generated by the PG phase. On the other hand, the PG energy scale $2\Delta_{PG}$ is defined as the frequency for which the dip just on the right side of the pair breaking peak ends. Remarkably, it is approximately at the same frequency as the one for which the PG depletion ends in the normal state [see Figs. 6(b) and 6(d) and Figs. 6(f) and 6(h)]. This is pointed out by the dashed line in the pairs of panels in Figs. 6(a) and 6(b) and 6(c) and 6(d), and Figs. 6(e) and 6(f) and 6(g) and 6(h). Note that this is not always the case.

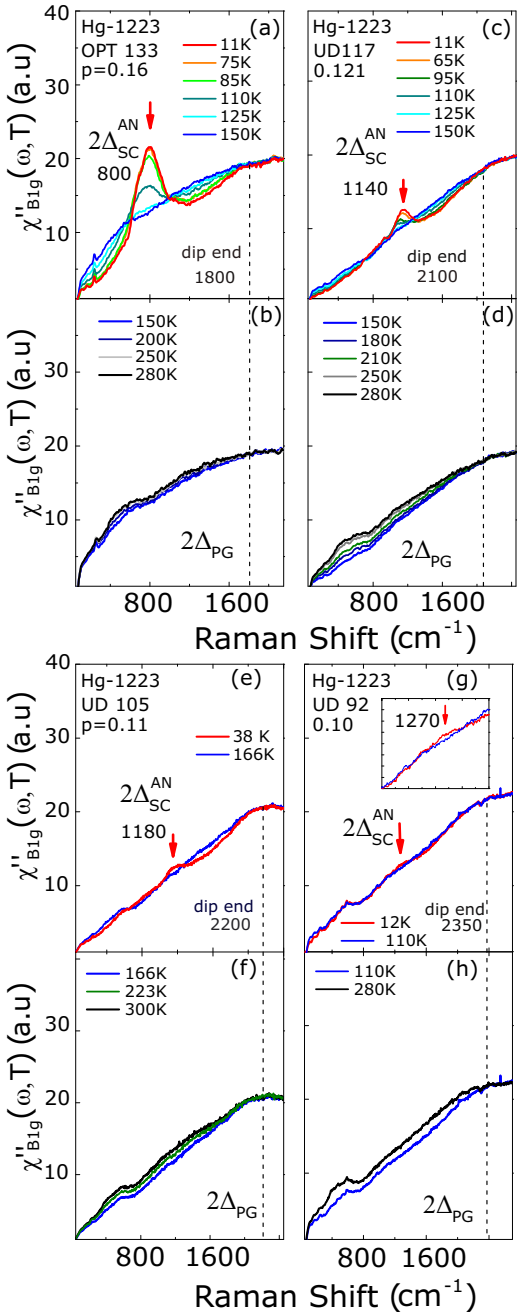

FIG. 6. (a) and (c) and (e) and (g): Temperature dependence of the B_{1g} Raman response function of Hg-1223 (with distinct doping levels) up to T_c. (b) and (d) and (f) and (h): Temperature dependence of the B_{1g} Raman response function of Hg-1223 (with distinct doping levels) above T_c. The pair breaking peak indicated by a red arrow determine the $2\Delta_{SC}^{AN}$ scale while the pseudogap $2\Delta_{PG}$ scale is defined from the energy for which the dip in the continuum ends. The inset in (d) corresponds to a zoom of the B_{1g} Raman response in order to point out the $2\Delta_{SC}^{AN}$.

2. Nodal superconducting and charge-density-wave energy scales

The temperature dependence of the B_{2g} Raman responses of the Hg-1223 compound for several doping levels are shown in Fig. 7. In Figs. 7(a) and 7(b) and Figs. 7(g) and 7(h) we detect both $2\Delta_{CDW}$ and the nodal SC gap $2\Delta_{SC}^{N}$.

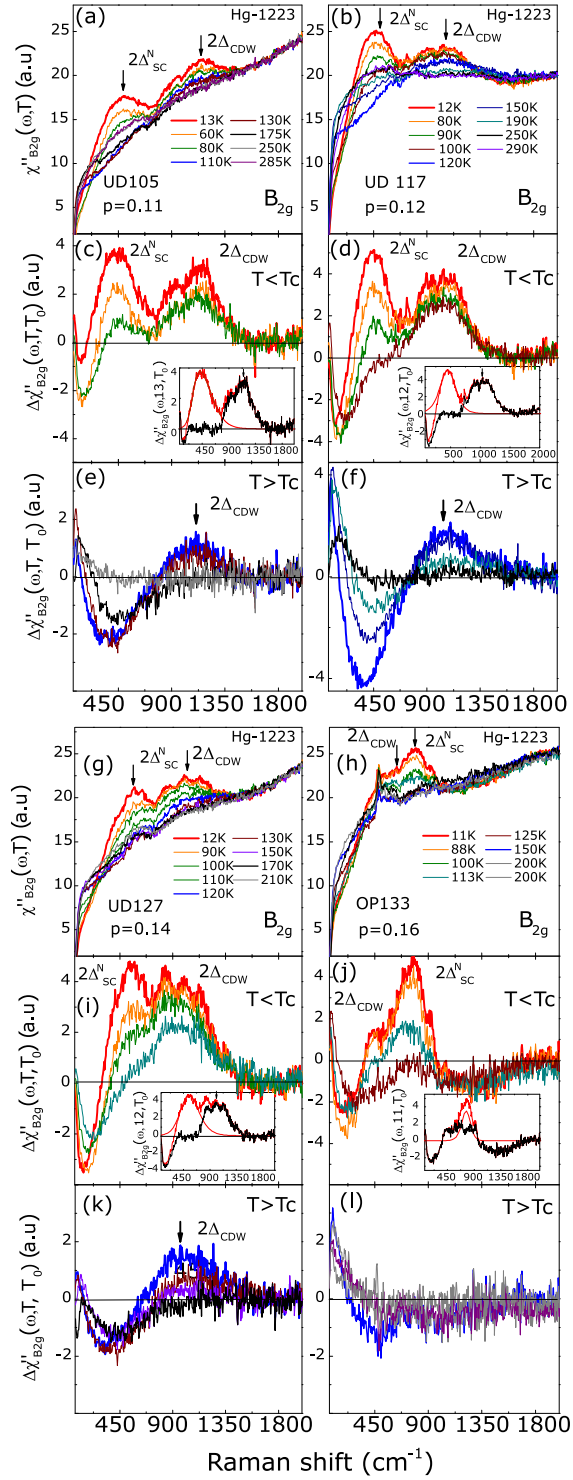

FIG. 7. (a) and (b) and (g) and (h): Temperature dependence of the nodal Raman responses (B_{2g}) of $HgBa_2Ca_2Cu_3O_{8+\delta}$ (Hg-1223) for several doping levels. The features related to the CDW and the nodal SC gap are indicated by black arrows. (c) and (d) and (h) and (j) : Nodal Raman responses below T_c, after subtracting the one at T_0. The T_0 values for each doping are listed in the text. In the insets the black curve corresponds to the CDW hump rid of the nodal SC component, the full red curve is a ASG fit of the SC nodal gap subtracted (see text for more details). (e) and (f) and (k) and (l): Nodal Raman responses above T_c, after subtracting the one at T_0 to highlight the CDW structure (dip and hump).

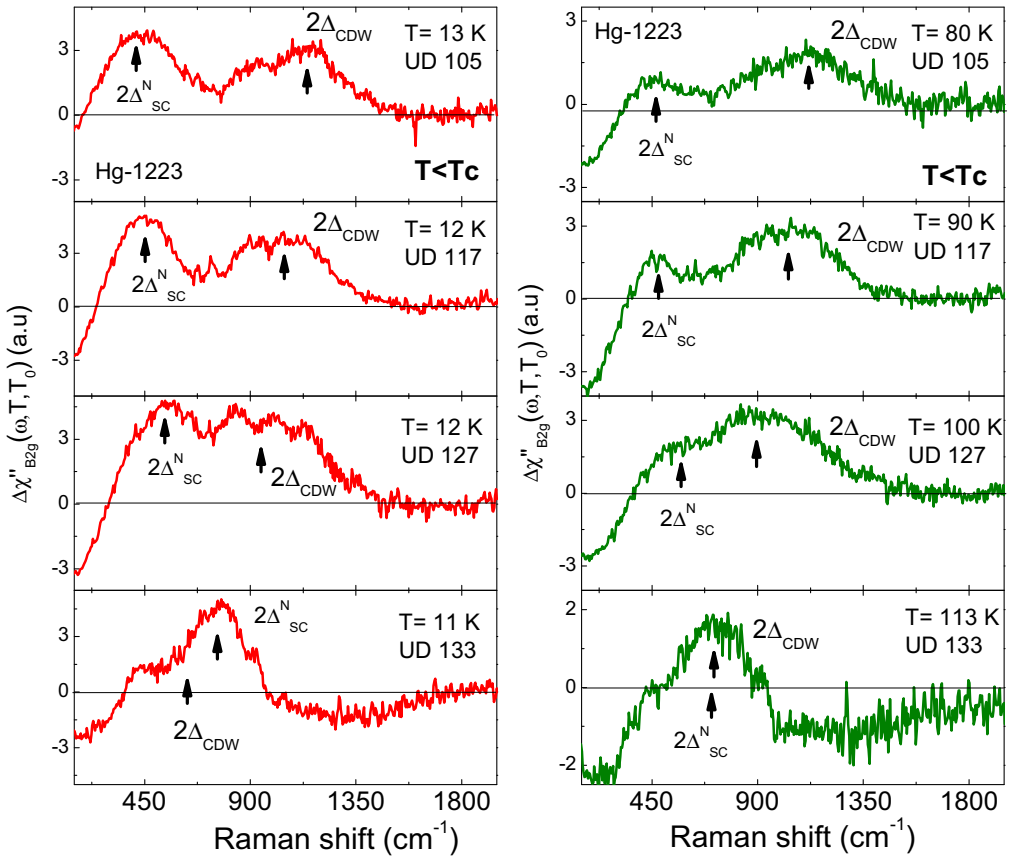

FIG. 8. Left and right panels are, respectively, the subtracted Raman responses of Hg-1223, $\Delta\chi''_{B_{2g}}(T \approx 12\ \text{K}, T_0)$ and $\Delta\chi''_{B_{2g}}$ $(T_c \approx 25\ \text{K}, T_0)$ for various doping levels. The T_0 values for each doping are listed in the text. The black arrows indicate the location of $\Delta_{\text{CDW}}(p)$ and $\Delta^{\text{N}}_{\text{SC}}(p)$. The red dotted line is just a guide for the eyes.

For $p = 0.11$, $2\Delta_{\text{CDW}}$ and $2\Delta^{\text{N}}_{\text{SC}}$ are well separated in frequency. However, as p increases, they are getting closer in frequency, and for $p = 0.16$, they are almost superimposed. In order to stress these two gaps, we plotted $\Delta\chi''_{B_{2g}}(\omega, T, T_0) = \chi''_{B_{2g}}(\omega, T) - \chi''_{B_{2g}}(\omega, T_0)$ where T_0 takes the values: 285, 290, 210, and 280 K for, respectively, UD 105, UD 117, UD 127, and OP 133 [see Figs. 7(c) and 7(d) and Figs. 7(h) and 7(j)]. As T increases up to T_c, the intensity of the nodal component of the SC gap is strongly reduced while the intensity of the CDW hump remains almost constant (see black arrows). We can bring out the CDW signal below T_c by taking off the SC nodal gap contribution after fitting it by an asymmetric Gaussian (AsG) function (see insets in Fig. 7). The set of the fitting parameters used for the doping levels $p = 0.11$, 0.12, 0.14, and 0.16 (at $T \approx 12$ K) are, respectively, ($A = 5$, $\omega_c = 441$ cm^{-1}, $\omega_1 = 292$ cm^{-1}, $\omega_2 = 47$ cm^{-1}, $\omega_3 = 116$ cm^{-1}), ($A = 13$, $\omega_c = 456$ cm^{-1}, $\omega_1 = 80$ cm^{-1}, $\omega_2 = 90$ cm^{-1}, $\omega_3 = 85$ cm^{-1}),($A = 8$, $\omega_c = 540$ cm^{-1}, $\omega_1 = 200$ cm^{-1}, $\omega_2 = 80$ cm^{-1}, $\omega_3 = 110$ cm^{-1}), and ($A = 7$, $\omega_c = 770$ cm^{-1}, $\omega_1 = 80$ cm^{-1}, $\omega_2 = 50$ cm^{-1}, $\omega_3 = 40$ cm^{-1}). Above T_c, the nodal SC gap $2\Delta^{\text{N}}_{\text{SC}}$ is gone and only remains the CDW gap: a dip-hump structure [see $\Delta\chi''_{B_{2g}}(\omega, T, T_0)$ in Figs. 7(e) and 7(f) and Figs. 7(k) and 7(l)]. Note that the CDW dip-hump structure is observable in the Raman spectra for $p = 0.11$, 0.12, and 0.14 while for $p = 0.16$ it is hardly detectable, likely because the CDW signal collapses below or close to $T_c = 133$ K. We can improve the determination of the $2\Delta_{\text{CDW}}(p)$ value by analyzing the nodal Raman responses at low temperature. However, the extraction of $2\Delta_{\text{CDW}}(p)$ is complicated by the existence of the SC signal. See the subtracted Raman response $\Delta\chi''_{B_{2g}}(\omega, T \approx 12\ \text{K}, T_0)$ of Hg-1223 (left panel of Fig. 8). The situation is even more complex for $p = 0.16$ where the Raman CDW signal coincides with the nodal SC one. Yet, if we increase T but stay below T_c, this allows us to weaken the SC signal and bring out the CDW signal and obtain reliable $2\Delta_{\text{CDW}}(p)$ values. This is achieved by measuring $\Delta\chi''_{B_{2g}}(\omega, T, T_0)$ with $T \approx 25$ K below T_c for each doping level (see right panel of Fig. 8). We then find that $2\Delta_{\text{CDW}} = 1150$, 1030, 930, and 730 cm^{-1} for, respectively, $p = 0.11$, 0.12, and 0.14 and $p = 0.16$. Note that this procedure is applicable because as it can be seen in Fig. 7, the location of CDW hump is almost temperature independent.

[1] B. Keimer, S. A. Kivelson, M. R. Norman, S. Uchida, and J. Zaanen, Nature (London) **518**, 179 (2015).

[2] J. Bednorz and K. Müller, Z. Phys. B Condens. Matter **64**, 189 (1986).

[3] J. Bardeen, L. N. Cooper, and J. R. Schrieffer, Phys. Rev. **108**, 1175 (1957).

[4] B. Loret, N. Auvray, Y. Gallais, M. Cazayous, A. Forget, D. Colson, M.-H. Julien, I. Paul, M. Civelli, and A. Sacuto, Nat. Phys. **15**, 771 (2019).

[5] G. Blumberg, M. Kang, M. V. Klein, K. Kadowaki, and C. Kendziora, Science **278**, 1427 (1997).

[6] M. Opel, R. Nemetschek, C. Hoffmann, R. Philipp, P. F. Muller, R. Hackl, I. Tutto, A. Erb, B. Revaz, E. Walker, H. Berger, and L. Forro, Phys. Rev. B **61**, 9752 (2000).

[7] M. Le Tacon, A. Sacuto, A. Georges, G. Kotliar, Y. Gallais, D. Colson, and A. Forget, Nat. Phys. **2**, 537 (2006).

[8] T. P. Devereaux and R. Hackl, Rev. Mod. Phys. **79**, 175 (2007).

[9] S. Blanc, Y. Gallais, M. Cazayous, M. A. Méasson, A. Sacuto, A. Georges, J. S. Wen, Z. J. Xu, G. D. Gu, and D. Colson, Phys. Rev. B **82**, 144516 (2010).

[10] S. Benhabib, A. Sacuto, M. Civelli, I. Paul, M. Cazayous, Y. Gallais, M. A. Méasson, R. D. Zhong, J. Schneeloch, G. D. Gu, D. Colson, and A. Forget, Phys. Rev. Lett. **114**, 147001 (2015).

[11] B. Loret, S. Sakai, S. Benhabib, Y. Gallais, M. Cazayous, M. A. Méasson, R. D. Zhong, J. Schneeloch, G. D. Gu, A. Forget, D. Colson, I. Paul, M. Civelli, and A. Sacuto, Phys. Rev. B **96**, 094525 (2017).

[12] B. Loret, Y. Gallais, M. Cazayous, R. D. Zhong, J. Schneeloch, G. D. Gu, A. Fedorov, T. K. Kim, S. V. Borisenko, and A. Sacuto, Phys. Rev. B **97**, 174521 (2018).

[13] M. R. Norman and C. Pépin, Rep. Prog. Phys. **66**, 1547 (2003).

[14] Provided the energy scale variations are not too large over different patches in which an electronic order sets in.

[15] Y. Li, M. Le Tacon, Y. Matiks, A. V. Boris, T. Loew, C. T. Lin, L. Chen, M. K. Chan, C. Dorow, L. Ji, N. Barišić, X. Zhao, M. Greven, and B. Keimer, Phys. Rev. Lett. **111**, 187001 (2013).

[16] V. J. Emery and S. A. Kivelson, Nature (London) **374**, 434 (1995).

[17] K. B. Efetov, H. Meier, and C. Pépin, Nat. Phys. **9**, 442 (2013).

[18] S. Sachdev and R. La Placa, Phys. Rev. Lett. **111**, 027202 (2013).

[19] E. Fradkin, S. A. Kivelson, and J. M. Tranquada, Rev. Mod. Phys. **87**, 457 (2015).

[20] Y. Wang, D. F. Agterberg, and A. Chubukov, Phys. Rev. Lett. **114**, 197001 (2015).

[21] S. Caprara, C. Di Castro, G. Seibold, and M. Grilli, Phys. Rev. B **95**, 224511 (2017).

[22] D. Chakraborty, M. Grandadam, M. H. Hamidian, J. C. S. Davis, Y. Sidis, and C. Pépin, Phys. Rev. B **100**, 224511 (2019).

[23] B. Loret, S. Sakai, Y. Gallais, M. Cazayous, M.-A. Méasson, A. Forget, D. Colson, M. Civelli, and A. Sacuto, Phys. Rev. Lett. **116**, 197001 (2016).

[24] R. Dipasupil, M. Oda, N. Momono, and M. Ido, J. Phys. Soc. Jpn. **71**, 1535 (2002).

[25] K. McElroy, D.-H. Lee, J. E. Hoffman, K. M. Lang, J. Lee, E. W. Hudson, H. Eisaki, S. Uchida, and J. C. Davis, Phys. Rev. Lett. **94**, 197005 (2005).

[26] J. C. Campuzano, H. Ding, M. R. Norman, H. M. Fretwell, M. Randeria, A. Kaminski, J. Mesot, T. Takeuchi, T. Sato, T. Yokoya, T. Takahashi, T. Mochiku, K. Kadowaki, P. Guptasarma, D. G. Hinks, Z. Konstantinovic, Z. Z. Li, and H. Raffy, Phys. Rev. Lett. **83**, 3709 (1999).

[27] P. A. Lee, N. Nagaosa, and X.-G. Wen, Rev. Mod. Phys. **78**, 17 (2006).

[28] R. Comin and A. Damascelli, Annu. Rev. Condens. Matter Phys. **7**, 369 (2016).

[29] A. Legros, B. Loret, A. Forget, P. Bonnaillie, G. Collin, P. Thuéry, A. Sacuto, and D. Colson, Mater. Res. Bull. **118**, 110479 (2019).

[30] H. Alloul, F. Rullier-Albenque, B. Vignolle, D. Colson, and A. Forget, Europhys. Lett. **91**, 37005 (2010).

[31] M. Bakr, S. M. Souliou, S. Blanco-Canosa, I. Zegkinoglou, H. Gretarsson, J. Strempfer, T. Loew, C. T. Lin, R. Liang, D. A. Bonn, W. N. Hardy, B. Keimer, and M. Le Tacon, Phys. Rev. B **88**, 214517 (2013).

[32] S. Benhabib, Y. Gallais, M. Cazayous, M.-A. Méasson, R. D. Zhong, J. Schneeloch, A. Forget, G. D. Gu, D. Colson, and A. Sacuto, Phys. Rev. B **92**, 134502 (2015).

[33] W. Guyard, A. Sacuto, M. Cazayous, Y. Gallais, M. Le Tacon, D. Colson, and A. Forget, Phys. Rev. Lett. **101**, 097003 (2008).

[34] N. Munnikes, B. Muschler, F. Venturini, L. Tassini, W. Prestel, S. Ono, Y. Ando, D. C. Peets, W. N. Hardy, R. Liang, D. A. Bonn, A. Damascelli, H. Eisaki, M. Greven, A. Erb, and R. Hackl, Phys. Rev. B **84**, 144523 (2011).

[35] Y. Toda, F. Kawanokami, T. Kurosawa, M. Oda, I. Madan, T. Mertelj, V. V. Kabanov, and D. Mihailovic, Phys. Rev. B **90**, 094513 (2014).

[36] A. Kaminski, T. Kondo, T. Takeuchi, and G. Gu, Philos. Mag. **95**, 453 (2015).

[37] In Y-123, $2\Delta_{\rm PG}(p)$ values were extracted from ellipsometry [54,55] and Raman [49] measurements, $2\Delta_{\rm SC}^{\rm AN}(p)$ from Raman [6,56], and $2\Delta_{\rm CDW}(p)$ from Raman [4]. In Hg-1201, $2\Delta_{\rm PG}(p)$ and $2\Delta_{\rm SC}^{\rm AN}(p)$ values were extracted from the B_{1g} SC Raman spectra [4,7,15,33,49,57] as detailed in the first section. We extracted the $2\Delta_{\rm CDW}(p)$ from the B_{2g} Raman spectra [4,15]. Note that we have re-interpreted the data of Li *et al.* [15] in the light of our recent works [4]. In Bi-2212, the $2\Delta_{\rm PG}(p)$ values come from Raman [49]. The $2\Delta_{\rm SC}^{\rm AN}(p)$ values were extracted from Raman [10,12,34,49,58]. In Y-123, Hg-1201, and Bi-2212 the $2\Delta_{\rm SC}^{\rm N}(p)$ values were extracted from Raman data stemming from Refs. [6,34,59], Refs. [4,7,15,33,57,60], and Refs. [10,34,58], respectively. In Hg-1223, T^* values were extracted from transport [61,62], infrared [63], and Raman [4], and $T_{\rm CDW}$ and T_c from Raman and magnetic susceptibility [4]. In Y-123, T^* values were extracted from ellipsometry [54], transport [64], and neutron [65] data, and $T_{\rm CDW}$ and T_c from x-ray and transport [28,66–68] and nuclear magnetic resonance (NMR) [69]. In Hg-1201, T^* values were extracted from Raman [57], neutron [70–72], and transport [73], and $T_{\rm CDW}$ and $T_{\rm c}$ from x ray and transport [74]. In Bi-2212, T^* and $T_{\rm c}$ values were extracted from transport [75,76], infrared [77], tunneling [24,78], ARPES [36,79], neutron[80], pump probe spectroscopy (PPS) [35], and Raman [10], $T_{\rm CDW}$ from x ray [81].

[38] P. W. Anderson, Science **235**, 1196 (1987).

[39] D. Scalapino, Phys. Rep. **250**, 329 (1995).

[40] G. Kotliar, Phys. Rev. B **37**, 3664 (1988).

[41] N. Bulut, D. J. Scalapino, and S. R. White, Phys. Rev. Lett. **72**, 705 (1994).

[42] B. Kyung, V. Hankevych, A.-M. Daré, and A.-M. S. Tremblay, Phys. Rev. Lett. **93**, 147004 (2004).

[43] B. Kyung, S. S. Kancharla, D. Sénéchal, A.-M. S. Tremblay, M. Civelli, and G. Kotliar, Phys. Rev. B **73**, 165114 (2006).

[44] B. Kyung, D. Sénéchal, and A.-M. S. Tremblay, Phys. Rev. B **80**, 205109 (2009).

[45] E. Gull, O. Parcollet, and A. J. Millis, Phys. Rev. Lett. **110**, 216405 (2013).

[46] W. Wu, M. Ferrero, A. Georges, and E. Kozik, Phys. Rev. B **96**, 041105(R) (2017).

[47] L. Fratino, P. Sémon, M. Charlebois, G. Sordi, and A.-M. S. Tremblay, Phys. Rev. B **95**, 235109 (2017).

[48] W. Wu, M. S. Scheurer, S. Chatterjee, S. Sachdev, A. Georges, and M. Ferrero, Phys. Rev. X **8**, 021048 (2018).

[49] B. Loret, A. Forget, J.-B. Moussy, S. Poissonnet, P. Bonnaillie, G. Collin, P. Thuéry, A. Sacuto, and D. Colson, Inorg. Chem. **56**, 9396 (2017).

[50] A. Bertinotti, J.-F. M. D. Colson, G. L. B. V. Viallet, L. Fruchter, C. Marcenat, and J. H. A. Carrington, *Hg-Based High T_c Superconductors*, edited by E. Narlikar (Nova Science, New York, 1997).

[51] M. R. Presland, J. L. Tallon, R. G. Buckley, R. S. Liu, and N. E. Flower, Physica C **176**, 95 (1991).

[52] J. Wen, Z. Xu, G. Xu, M. Hücker, J. Tranquada, and G. Gu, J. Cryst. Growth **310**, 1401 (2008), the Proceedings of the 15th International Conference on Crystal Growth (ICCG-15) in conjunction with the International Conference on Vapor Growth and Epitaxy and the U.S. Biennial Workshop on Organometallic Vapor Phase Epitaxy.

[53] L. Mihaly, C. Kendziora, J. Hartge, D. Mandrus, and L. Forro, Rev. Sci. Instrum. **64**, 2397 (1993).

[54] C. Bernhard, L. Yu, A. Dubroka, K. Kim, M. Rössle, D. Munzar, J. Chaloupka, C. Lin, and T. Wolf, J. Phys. Chem. Solids **69**, 3064 (2008).

[55] A. Dubroka, M. Rössle, K. W. Kim, V. K. Malik, D. Munzar, D. N. Basov, A. A. Schafgans, S. J. Moon, C. T. Lin, D. Haug, V. Hinkov, B. Keimer, T. Wolf, J. G. Storey, J. L. Tallon, and C. Bernhard, Phys. Rev. Lett. **106**, 047006 (2011).

[56] T. Masui, M. Limonov, H. Uchiyama, S. Lee, S. Tajima, and A. Yamanaka, Phys. Rev. B **68**, 060506(R) (2003).

[57] W. Guyard, M. Le Tacon, M. Cazayous, A. Sacuto, A. Georges, D. Colson, and A. Forget, Phys. Rev. B **77**, 024524 (2008).

[58] F. Venturini, M. Opel, R. Hackl, H. Berger, L. Forró, and B. Revaz, J. Phys. Chem. Solids **63**, 2345 (2002).

[59] S. Sugai, H. Suzuki, Y. Takayanagi, T. Hosokawa, and N. Hayamizu, Phys. Rev. B **68**, 184504 (2003).

[60] Y. Gallais, M. L. Tacon, A. Sacuto, and D. Colson, Europhys. Lett. **73**, 594 (2006).

[61] A. Carrington, D. Colson, Y. Dumont, C. Ayache, A. Bertinotti, and J. Marucco, Physica C **234**, 1 (1994).

[62] M.-H. Julien, P. Carretta, M. Horvatić, C. Berthier, Y. Berthier, P. Ségransan, A. Carrington, and D. Colson, Phys. Rev. Lett. **76**, 4238 (1996).

[63] J. J. McGuire, M. Windt, T. Startseva, T. Timusk, D. Colson, and V. Viallet-Guillen, Phys. Rev. B **62**, 8711 (2000).

[64] R. Daou, J. Chang, D. LeBoeuf, O. Cyr-Choinière, F. Laliberté, N. Doiron-Leyraud, B. J. Ramshaw, R. Liang, D. A. Bonn, W. N. Hardy, and L. Taillefer, Nature (London) **463**, 519 (2010).

[65] Y. Sidis and P. Bourges, J. Phys. Conf. Ser. **449**, 012012 (2013).

[66] S. Blanco-Canosa, A. Frano, E. Schierle, J. Porras, T. Loew, M. Minola, M. Bluschke, E. Weschke, B. Keimer, and M. Le Tacon, Phys. Rev. B **90**, 054513 (2014).

[67] M. Hücker, N. B. Christensen, A. T. Holmes, E. Blackburn, E. M. Forgan, R. Liang, D. A. Bonn, W. N. Hardy, O. Gutowski, M. v. Zimmermann, S. M. Hayden, and J. Chang, Phys. Rev. B **90**, 054514 (2014).

[68] R. Arpaia, S. Caprara, R. Fumagalli, G. De Vecchi, Y. Y. Peng, E. Andersson, D. Betto, G. M. De Luca, N. B. Brookes, F. Lombardi, M. Salluzzo, L. Braicovich, C. Di Castro, M. Grilli, and G. Ghiringhelli, Science **365**, 906 (2019).

[69] T. Wu, H. Mayaffre, S. Krämer, M. Horvatić, C. Berthier, W. N. Hardy, R. Liang, D. A. Bonn, and M.-H. Julien, Nat. Commun. **6**, 6438 (2015).

[70] Y. Li, V. Balédent, N. Barišić, Y. Cho, B. Fauque, Y. Sidis, G. Yu, X. Zhao, P. Bourges, and M. Greven, Nature (London) **455**, 372 (2008).

[71] V. Balédent, D. Haug, Y. Sidis, V. Hinkov, C. T. Lin, and P. Bourges, Phys. Rev. B **83**, 104504 (2011).

[72] Y. Li, V. Balédent, N. Barišić, Y. C. Cho, Y. Sidis, G. Yu, X. Zhao, P. Bourges, and M. Greven, Phys. Rev. B **84**, 224508 (2011).

[73] N. Barisic, M. K. Chan, Y. Li, G. Yu, X. Zhao, M. Dressel, A. Smontara, and M. Greven, Proc. Natl. Acad Sci. USA **110**, 12235 (2013).

[74] W. Tabis, B. Yu, I. Bialo, M. Bluschke, T. Kolodziej, A. Kozlowski, E. Blackburn, K. Sen, E. M. Forgan, M. v. Zimmermann, Y. Tang, E. Weschke, B. Vignolle, M. Hepting, H. Gretarsson, R. Sutarto, F. He, M. Le Tacon, N. Barišić, G. Yu, and M. Greven, Phys. Rev. B **96**, 134510 (2017).

[75] T. Watanabe, T. Fujii, and A. Matsuda, Phys. Rev. Lett. **79**, 2113 (1997).

[76] T. Usui, D. Fujiwara, S. Adachi, H. Kudo, K. Murata, H. Kushibiki, T. Watanabe, K. Kudo, T. Nishizaki, N. Kobayashi, S. Kimura, K. Yamada, T. Naito, T. Noji, and Y. Koike, J. Phys. Soc. Jpn. **83**, 064713 (2014).

[77] J. Hwang, T. Timusk, and G. D. Gu, Nature (London) **427**, 714 (2004).

[78] L. Ozyuzer, J. F. Zasadzinski, K. E. Gray, C. Kendziora, and N. Miyakawa, Europhys. Lett. **58**, 589 (2002).

[79] I. M. Vishik, M. Hashimoto, R.-H. He, W.-S. Lee, F. Schmitt, D. Lu, R. G. Moore, C. Zhang, W. Meevasana, T. Sasagawa, S. Uchida, K. Fujita, S. Ishida, M. Ishikado, Y. Yoshida, H. Eisaki, Z. Hussain, T. P. Devereaux, and Z.-X. Shen, Proc. Natl. Acad. Sci. USA **109**, 18332 (2012).

[80] L. Mangin-Thro, Y. Sidis, P. Bourges, S. De Almeida-Didry, F. Giovannelli, and I. Laffez-Monot, Phys. Rev. B **89**, 094523 (2014).

[81] E. H. da Silva Neto, P. Aynajian, A. Frano, R. Comin, E. Schierle, E. Weschke, A. Gyenis, J. Wen, J. Schneeloch, Z. Xu, S. Ono, G. Gu, M. Le Tacon, and A. Yazdani, Science **343**, 393 (2014).